Chemistry of surface nanostructures in lead precursor-rich PbZr 0.52 Ti 0.48 O 3 sol-gel films

I Gueye, G Le Rhun, P Gergaud, O Renault, E Defay, N Barrett

Chemistry of surface nanostructures in lead precursor-rich $PbZr_{0.52}Ti_{0.48}O_3$ sol-gel films

I. Gueye, G. Le Rhun, P. Gergaud, O. Renault

Univ. Grenoble Alpes, F-38000 Grenoble, France and CEA, LETI, MINATEC Campus, F-38054 Grenoble, France.

E. Defay

Luxembourg Institute of Science and Technology, Materials Research and Technology Department, 41 Rue du Brill, L-4422 Belvaux, Luxembourg.

N. Barrett

SPEC, CEA, CNRS, Universit Paris Saclay, F-91191 Gif-sur-Yvette, France

Abstract

We present a study of the chemistry of the nanostructured phase at the surface of lead zirconium titanate $PbZr_{0.52}Ti_{0.48}O_3$ (PZT) films synthesized by sol-gel method. In sol-gel synthesis, excess lead precursor is used to maintain the target stoichiometry. Surface nanostructures appear at 10% excess lead precursor whereas 30% excess precursor inhibits their formation. Using the surface-sensitive, quantitative X-ray photoelectron spectroscopy and glancing angle X-ray diffraction we have shown that the chemical composition of the nanostructures is $ZrO_{1.82-1.89}$ rather than pyrochlore often described in the literature. The presence of a possibly discontinuous layer of wide band gap $ZrO_{1.82-1.89}$ could be of importance in determining the electrical properties of PZT-based metal-insulator-metal heterostructures.

Keywords: PZT, X-ray photoelectron spectroscopy, Surface phase, Diffraction, SEM

Email address: nick.barrett@cea.fr (N. Barrett)

1. Introduction

Lead zirconium Titanate $Pb(Zr_xTi_{1-x})O_3$ (PZT) is widely used in applications such as microelectromechanical systems (MEMS), piezoelectric actuators [1], ferroelectric nonvolatile memories [2], infrared pyroelectric detectors [3], and decoupling capacitors. Capacitor device performances in particular are determined not only by the bulk dielectric properties which depend on the stoichiometry and the manufacturing process but also by the interface with the electrodes. PZT exhibits optimal dielectric and piezoelectric response near to the morphotropic phase boundary with a Zr/Ti ratio of 52/48 (i.e. $PbZr_{0.52}Ti_{0.48}O_3$ or PZT (52/48)) [4]. Sol-gel synthesis is well adapted for mass production of PZT but lead loss produced during the necessary crystallization annealing [5] requires excess lead precursor for obtaining the near stoichiometric values [6]. This may also lead to changes in surface composition and hence modifications of the PZT/electrode interface chemistry. Surface phases have been observed [7, 8] which appear dependent on the excess Pb content [9] and growth process [10, 11]. However, little is known about their chemistry and even less regarding their effect on device performance.

The secondary phase at the PZT surface has been studied using X-ray diffraction (XRD) [12, 13, 14]. It has been suggested that the phase observed at the surface of PZT thin films after crystallization is of pyrochlore type ($A_2B_2O_{7-x}$) [14, 15]. Pyrochlore is produced mainly at lower temperature and vanishes as temperature increases [9, 12, 10]. However, other possible phases have also been suggested, such as PbO [11], fluorite [16, 17] or ZrO_2 [18]. Therefore, the first question is to determine the chemical nature of eventual secondary phases at the surface of sol-gel PZT.

In this paper, we present a detailed study of the surface chemistry of technologically-relevant, sol-gel synthetized PZT films by scanning electron microscopy (SEM), X-ray diffraction (XRD) and quantitative X-ray photoelectron spectroscopy (XPS). We investigate the role of lead excess on the surface composition, chemistry and micro-structure of PZT (52/48) thin films. In particular, we exploit the surface chemical sensitivity of XPS to identify the chemistry of the secondary surface phase. In contrast with some of the previous literature [19] we show that the surface phase is not pyrochlore but in fact consists of zirconium oxide nanostructures.

2. Experiment

The substrates are 200 mm silicon wafers. Thermal SiO_2 is grown at 1100°C in oxygen. A TiO_2 layer is obtained by depositing 10 nm of Ti followed by annealing at 700°C in oxygen for 30 min. TiO_2 is both an adhesion layer for the Pt electrode on SiO_2 and a lead diffusion barrier. The 100 nm bottom Pt electrode is sputter deposited at 450°C. The final bottom electrode/substrate heterostructure is hence Pt(111) 100 nm/TiO_2 20 nm/SiO_2 500 nm/Si 750 μm.

PZT layers were grown using the sol-gel technique [20]. 220 nm thick PZT films were grown, corresponding to 4 such layers. Each layer of PZT is spun, dried at 130°C and calcinated at 360°C. A rapid thermal annealing (RTA) step is performed at 700°C for 1 min under oxygen atmosphere after calcination of the 1st and 4th layers. This step enables crystallization of the PZT film in the perovskite structure. Two PZT samples were prepared for this study. The first one made of 4 layers with 10% ($Pb_{1.1}Zr_{0.52}Ti_{0.48}O_3$) lead precursor excess is hereafter referred to as PZT10. The second one made of 2 layers with 10% ($Pb_{1.1}Zr_{0.52}Ti_{0.48}O_3$) lead precursor excess in sandwich between 2 layers with 30% ($Pb_{1.3}Zr_{0.52}Ti_{0.48}O_3$) lead precursor excess is hereafter referred to as PZT30. Each sol-gel layer has a Zr/Ti composition gradient, with Ti maximum at the start of and Zr maximum at the end of each layer.

XPS analysis was carried out at a base pressure 5×10^{-10} mbar in a Multiprobe system (ScientaOmicron) fitted with a monochromatized Al Kα source (1486.6 eV) and a 128-channel, parallel detection Argus electron analyzer. In order to distinguish the contribution of the surface and sub-surface layers, we varied the photoelectron take-off angle (defined as the angle between the analyzer axis and the sample surface) from 90° (normal emission) to 30° ("grazing" or surface sensitive emission). The samples were mounted with double-side conductive tape onto the metallic sample holder. We checked that this mounting was electrically equivalent to grounding the PZT surface with silver paste.

The overall energy resolution (X-ray source bandwidth and spectrometer broadening) was 0.27 eV for the core-level spectra. The binding energy scale was calibrated using the C 1s binding energy. CasaXPS software was used for data analysis [21]. Shirley background and Gaussian-Lorentzian (70%-30%) line-shapes were used for the curve fitting process. The full-width at half maximum (FWHM) for each given emission line was constant.

XRD (θ-2θ) was performed using a XPERT-PRO MRD XL from PANALYTICAL, using Cu Kα radiation (λ=0.15418 nm). In-plane X-ray diffraction (GID) was also carried out to obtain information regarding surface crystallography. When the incident beam is close to or below the critical angle for total external reflection surface sensistivity is enhanced. The in-plane diffraction measurements were performed on a Smartlab Rigaku 5-circles, using an incidence angle ($\alpha_{\rm i}$) of 0.5°. The diffracted X-ray beam (2θ) is recorded for an azimuthal range from 15 to 65° while keeping the angle α_f of 0.5° constant with respect to the sample surface. The theoretical critical angle for total external reflection [22, 23] of 0.40° agrees well with the experimental value (0.36°). We therefore estimate an incidence angle 0.5° which corresponds to a penetration depth of around 38 nm for characterizing the nanostructures. As we will see this is quite suitable for detection of the nanostructures at the PZT surface.

SEM was carried out in the secondary electron (SE) detection mode with a Hitachi-4160 scanning electron microscope (30kV primary electron beam, 15 mA emission current and chamber pressure $\sim 10^{-7}$ mbar).

Ion beam etching (IBE) was performed to explore further the surface composition and presence of secondary phases using the NEXUS 350A apparatus at 7×10^{-4} mbar.

3. Results

3.1. Scanning electron microscopy

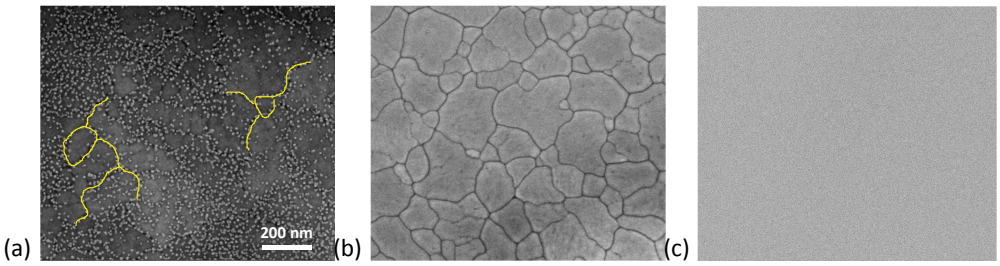

Figure 1: SEM images of (a) PZT10 as deposited, (b) PZT30 and (c) PZT10 after ion beam etching. The scale bar is the same for all three images.

Figure 1 shows the surface microstructure of (a) PZT10 as deposited, (b) PZT30 and (c) PZT10 after ion beam etching. The PZT30 sample has large

grains distributed over the whole surface with well-defined grain boundaries. The grain size varies from 40 nm to 250 nm diameter. The surface is clean with no other visible morphology. The surface of as deposited PZT10 has a similar underlying grain structure of comparable size to that of PZT30 but, in addition, is covered by a large number of much smaller structures. The size of these nanostructures varies between 5 and 25 nm with an average size over the field of view of 15 nm and they cover 10% of the total surface (Fig. 1(a)). A closer inspection suggests that they tend to be predominantly located along grain boundaries (indicated by the yellow lines in Fig. 1(a)) rather than in the center of the big grains. On the other hand, the PZT10 after 45s of etching reveals a perfectly smooth surface, without any small or large grains Fig. 1c) [24]. Etching has therefore removed the nanostructures. The lack of contrast between large grains suggests that the surface has also become amorphous due to the etching damage [20]. The etching damage and nanostructure removal are supported by the XPS results presented below.

3.2. X-ray photoelectron spectroscopy

Figure 2 shows the XPS survey spectra for the PZT10 and PZT30 samples. All the expected emission lines from Pb, Zr, Ti, O are detected. The C 1s peak reflects the presence of adventitious surface carbon. This was confirmed by depth profiling using Ar ion beam sputtering and Auger electron spectroscopy (not shown) which confirmed that all carbon was removed after etching 2.6 nm. Compared to the average size of the nanostructures this clearly shows that the carbon is only a surface contamination and is not intrinsic to the bulk of the sol-gel films. From the measured peak area and the Relative Sensitivity Factors (RSF, provided by ScientaOmicron), we can estimate the relative carbon concentration at the sample surface to be 22.1 and 12.2 atomic % for PZT30 and PZT10, respectively, i.e. up to one carbon atom per unit cell. However, this post-growth contamination does not affect the PZT surface structure or composition.

3.2.1. Core level spectra of as-received films.

The Pb 4f, Ti $2p_{3/2}$, Zr 3d and O 1s core level spectra recorded at normal emission are shown in Fig. 3(a-d) and the results of the best fits to the data are given in table I. The Pb $4f_{7/2}$ binding energy (137.5 eV) is identical for both samples. The single Pb component is attributed to Pb^{2+} ions in the PZT perovskite structure. No other chemical state of Pb is observed. Similarly, the Ti $2p_{3/2}$ binding energy (457.2 eV) is also unchanged between

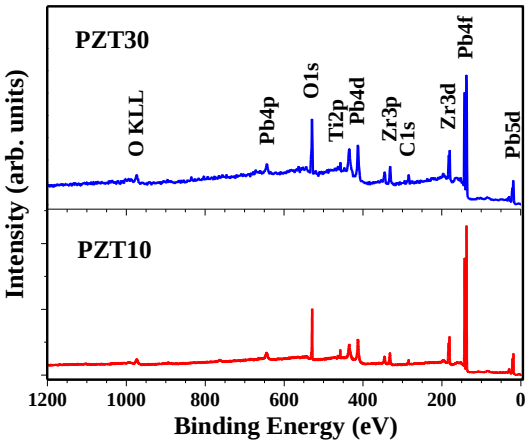

Figure 2: XPS survey spectra of PZT30 (top) and PZT10 (bottom).

PZT30 and PZT10 and is attributed to Ti^{4+} ions in the PZT matrix. The FWHM of the Pb $4f_{7/2}$ and the Ti $2p_{3/2}$ emission are 0.89 eV and 0.73 eV, respectively.

The Zr core level spectrum, shown in Fig. 3(c), changes dramatically between 10% and 30% lead excess. For the PZT30 sample, it shows a single chemical state labelled Zr_I with a Zr $3d_{5/2}$ binding energy of 180.5 eV. In contrast, for 10% lead excess, there is an additional component denoted Zr_{II} at 181.5 eV binding energy. Zr_I, common to both PZT30 and PZT10, is related to Zr^{4+} ions in the PZT perovskite structure. Zr_{II}, shifted by 1 eV to higher binding energy, seems to be correlated with the appearance of nanostructures at the surface of PZT10, as seen in Fig. 1(a). This suggests a different chemical composition of nanostructures with respect to that of PZT.

The O $1s$ spectra have several distinct core level components. The main peak, O_I at 528.70 eV is attributed to oxygen in the PZT perovskite structure and is common to both PZT10 and PZT30. For PZT10 there is a second peak at 529.40 eV. The peak O_{III} is present in both samples and attributed to surface contamination [21, 25]. Finally, peak O_{IV} at 531.6 eV is present only in the PZT30 spectrum.

In order to clarify the assignment of the Zr_{II} component to a surface secondary phase, we performed XPS on the PZT10 at a grazing take-off angle of 30° providing twofold enhancement of surface sensitivity. The corresponding Pb $4f$, Ti $2p_{3/2}$, Zr $3d$ and O $1s$ core level spectra are shown in Fig. 4(a-d),

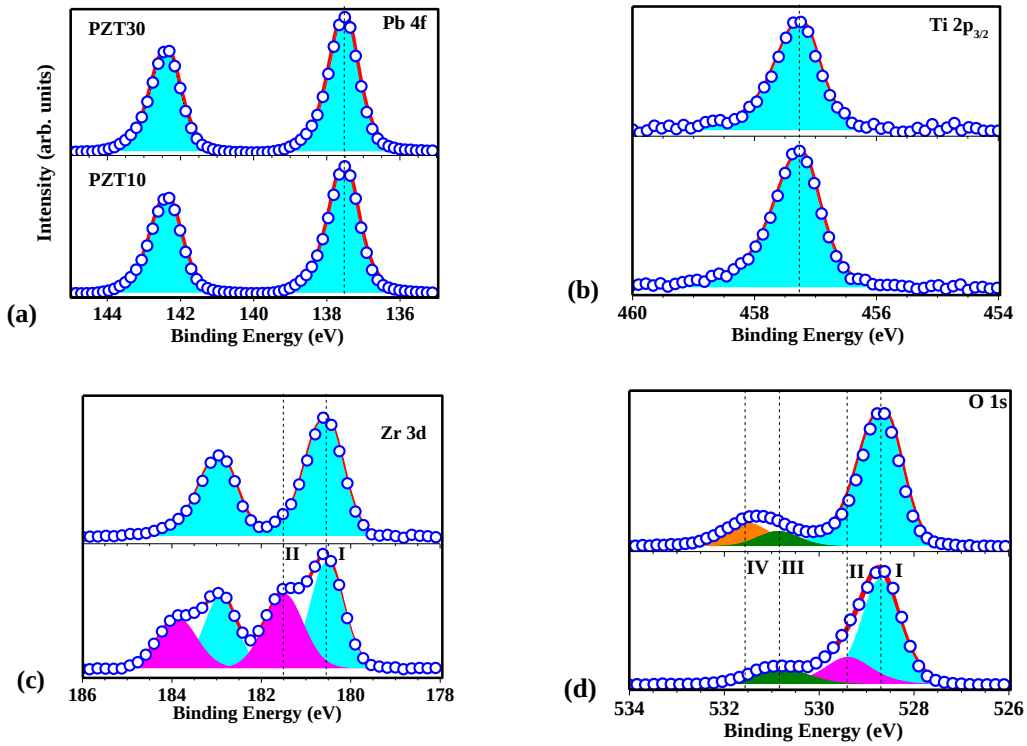

Figure 3: XPS core level spectra for a) Pb $4f$; b) Ti $2p_{3/2}$ c) Zr $3d$ and d) O $1s$. Open circles are the experimental points, red lines the best fit, colored peaks the different components. In each panel, the upper (lower) spectrum is that of PZT30 (PZT10). The main peak I (light gray, turquoise online) is the perovskite structure; gray peak II (magenta online) surface phase and low intensity, peaks III and IV (green and orange online) surface contaminations.

and compared with the normal emission case. No change in binding energy is observed as a function of take-off angle, only the relative intensities of the Zr and O core level components I and II vary.

At 30° the Zr_{II} intensities increase significantly relative to the Zr_{I} component (by 48% with respect to normal emission), in good agreement with the expected enhanced surface sensitivity at 30° take-off angle (probing depth is halved). The same twofold increase is observed for the O_{II} peak. At 30° take-off angle the OII intensity increases by 49% with respect to the intensity at normal emission. As the only effect of changing the take-off angle is to change the surface sensitivity, this is clear evidence that both Zr and O are

Table 1: Pb $4f_{7/2}$, Ti $2p_{3/2}$, Zr $3d_{5/2}$ and O $1s$ binding energies and FWHM, both in eV, of the fits shown in Fig. 4 for PZT10 and PZT30

Core-Level	PZT10		PZT30	
	BE	fwhm	BE	fwhm
Pb $4f_{7/2}$	137.5	0.89	137.5	0.89
Ti $2p_{3/2}$	457.2	0.73	457.2	0.73
Zr $3d_{3/2}$ (I)	180.5	0.85	180.5	0.85
Zr $3d_{3/2}$ (II)	181.5	1.02	-	-
O $1s$ (I)	528.7	0.95	528.7	0.95
O $1s$ (II)	529.4	1.18	-	-

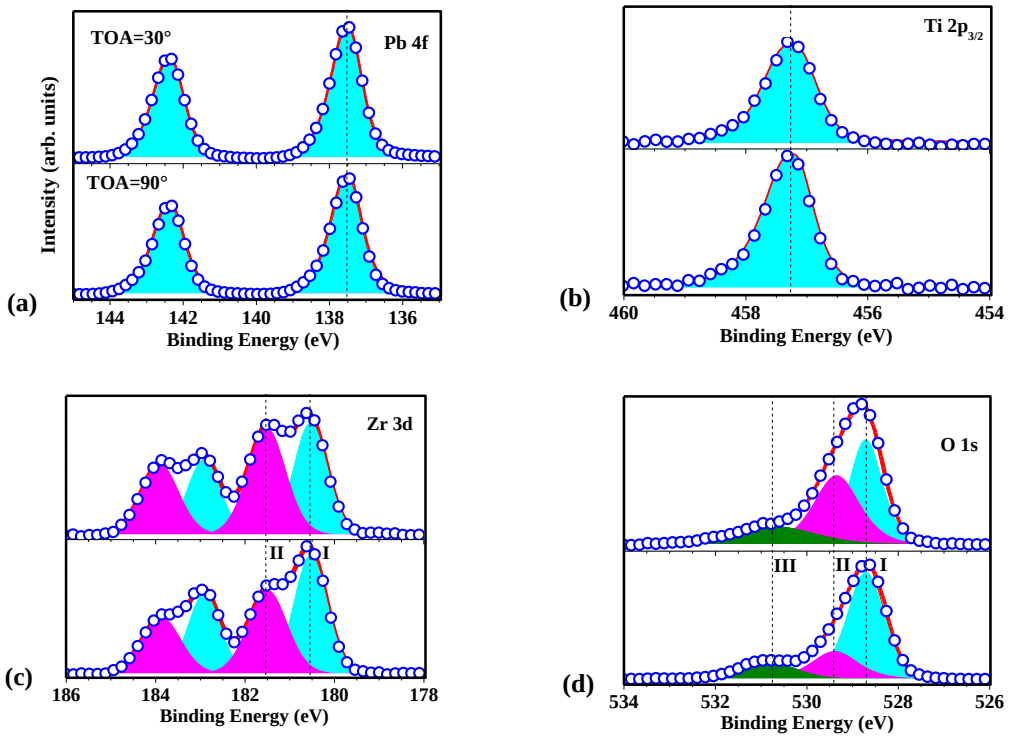

Figure 4: XPS ore level spectra of PZT10 as a function of take-off angle a) Pb$4f$; b) Ti$2p_{3/2}$ c) Zr$3d$ and d) O$1s$. Symbols and color code as in Fig. 3.

related to a surface specific phase. We can therefore conclude that both Zr_{II} and O_{II} are surface-related peaks and relate these with the appearance of nanostructures observed at the surface of PZT10.

3.2.2. Ion beam etching.

After IBE, the surface is smooth without any detectable nanostructure, as can be seen in Fig. 1(c), therefore the etching treatment has removed the additional surface phase. The absence of a clear grain structure is due to the IBE-induced amorphization of the surface, well-known in the literature [24, 20, 26]. IBE can also reduce the surface [17, 26] in which case one would expect a shift in the electronic levels similar to that induced by n-type doping of semiconductors. In order to compare the core level spectra before and after IBE we must first correct the energy scale for the electronic effect resulting from n-doping.

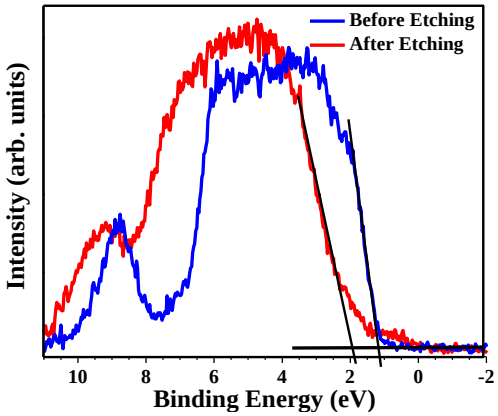

Figure 5: Valence band maxima of PZT 10 before (blue) and after IBE (red).

This is illustrated in Fig. 5 which shows the valence band spectra before and after etching. The position of the valence band maximum (VBM) is determined by a straight line extrapolation [27]. After etching, the VBM shifts from 1.17 to 1.94 eV and a density of states in the band gap appears. The latter is associated with the creation of oxygen vacancies which, schematically, donate 2 free electrons to the PZT lattice, reducing neighboring B-type cations, usually Ti. The resulting n-type doping pins the Fermi level near the bottom of the conduction band resulting in a rigid shift of all the electronic levels to higher binding energy. In order to compare the chemical information in the core level spectra we therefore aligned the core level spectra using the VBMs.

In Fig. 6, we compare the Pb $4f$, Ti $2p_{3/2}$, Zr $3d$ and O1s core level spectra, before and after IBE. The VBM aligned spectra show almost no change

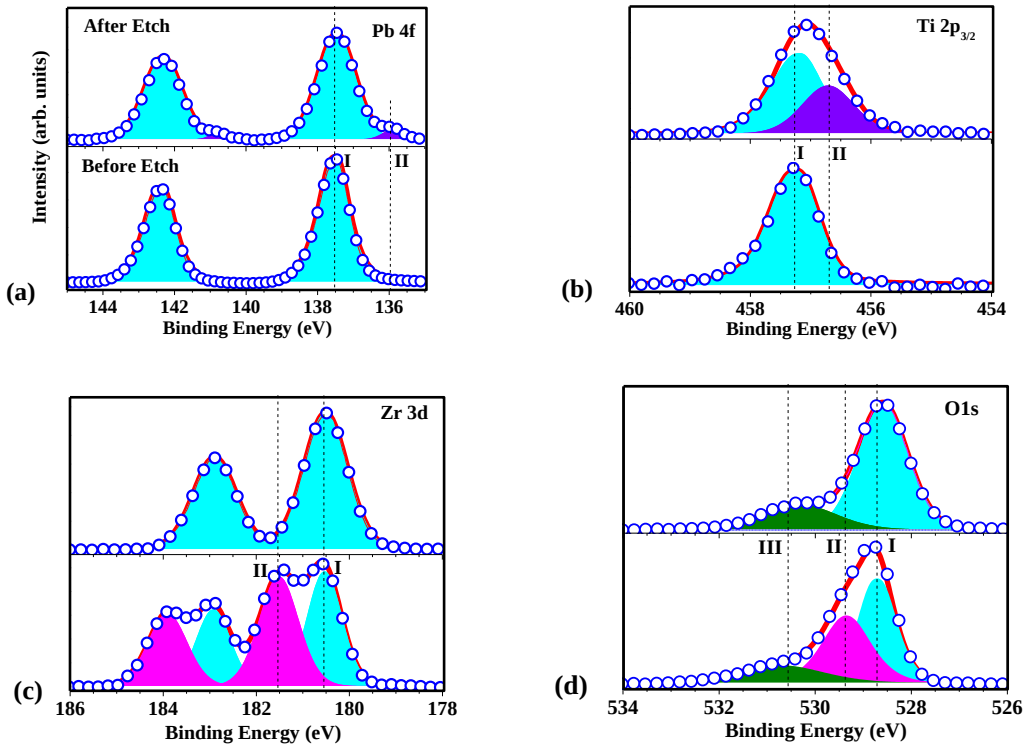

Figure 6: PZT10 a) Pb $4f$; b) Ti $2p_{3/2}$ c) Zr $3d$ and d) O $1s$ core level spectra before and after ion beam etching. Open circles are the experimental points, continuous (red) lines the best fit. Color coding of the core level components as for Fig. 3.

in binding energy, confirming the rigid nature of the etching induced shift. In the Pb $4f$ spectrum a new component at lower binding energy appears, and corresponds to metallic Pb^0 at 136.07 eV such as described by Lu and Zhu [28]; similarly, a partial reduction of Ti is evidenced with an additional component to lower binding energy (Ti_{II}) at 456.64 eV), as also observed previously [17]. Both results provide chemical confirmation of the surface reduction after IBE. On the other hand, and more importantly, the surface-related components Zr_{II} and O_{II} disappear after etching. IBE removed an estimated 20 nm thickness of PZT, i.e, well above the photoelectron escape depth; we can conclude that the Zr_{II} and O_{II} components observed before etching are directly correlated with the surface nanostructures. Finally, we observe a broadening of FWHM of about 0.2 eV for all spectra of PZT after etching. This is probably due to IBE induced surface amorphization,

responsible for the absence of grain contrast in Fig. 1c.

3.3. X-ray diffraction

The θ-2θ scans in Fig. 7 show up peaks characteristic of PZT, the Si substrate and the Pt electrode. The XRD also reveals several structural differences between PZT10 and PZT30. With 10% lead excess during deposition, the sample is almost fully (100) oriented. Increasing the lead excess from 10 to 30% leads to a modification of the structure since the PZT film is then strongly (111) oriented. There is also the appearance of a new peak at 31.2° corresponding to the PZT (110). Assuming equivalent scattering factors we estimate the proportion of (100), (110) and (111) oriented film to be, respectively, 93.2, 2.6 and 4.2 % for PZT 10 and 18.4, 21.5 and 60.2 % for PZT30.

The in-plane diffraction measurements at an incidence angle 0.5° have a depth sensitivity of 38nm close to the size of the nanograins. Figure 7b shows that in addition to the crystallographic orientation of the PZT, we observe three peaks respectively at 34, 58 and 61.5° in PZT10 which will be attributed to the surface phase. There is also one peak at 28° for both samples which corresponds to the relatively intense K_β stimulated peak of the PZT (110).

4. Discussion

As seen in Fig. 1(a), 10% of lead excess leads to the formation of surface nanostructures, preferentially localized at the grain boundaries. This secondary phase has been attributed to the incomplete reaction of ZrO_2 precursor [29] resulting from the opposite slopes in the concentration gradients of Ti and Zr during the growth of sol-gel layers [30, 31] The major portion of Ti incorporated into each layer is consumed at the beginning of nucleation, consistent with the known crystallization temperatures. This process leads to a dramatic reduction of Ti surface concentration and concomitant increase of Zr as seen from the quantitative analysis of the XPS data in Table II. The TiO_2 precursor is consumed at the beginning of the sol-gel layer growth and as a consequence the surface of the layer is strongly Zr-enriched. The complete reaction for the growth of lead zirconate titanate can be written in two stages: $PbO+TiO_2 \longrightarrow PbTiO_3$, followed by $PbTiO_3+PbO+ZrO_2 \longrightarrow Pb(Zr_{1-x},Ti_x)O_3$, where the initial precursors are PbO, TiO_2 and ZrO_2 [29].

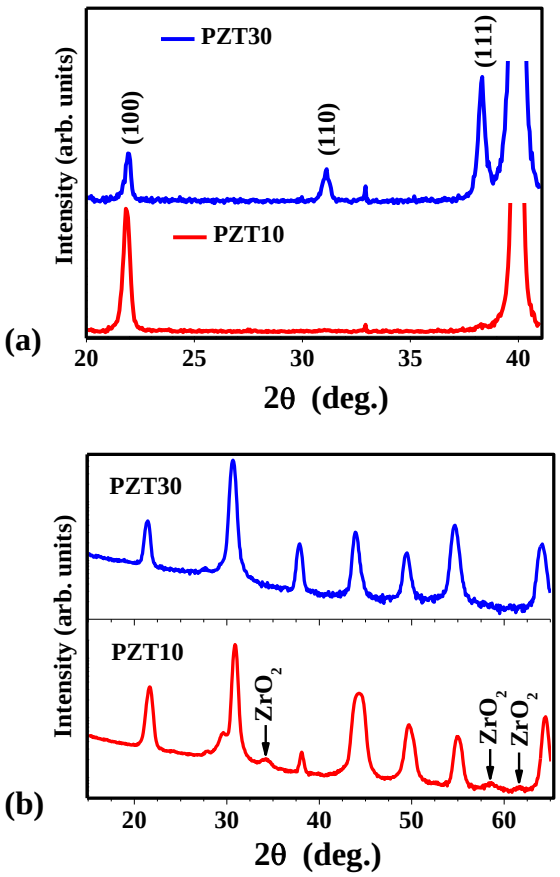

Figure 7: XRD scans at (a) θ-2θ and (b)grazing incidence of PZT10 (bottom, red) and PZT30 (top, blue)

Using the RSFs we can quantify the surface stoichiometry as measured by XPS. The quantification reveals several important features. First, there is slight Pb enrichment at the surface for both PZT10 and PZT30. This is to be expected since excess Pb is used in both cases, as can be seen simply from the overall proportion of Pb, in both cases greater than the stoichiometric value of 20%. As expected, the surface enrichment is stronger for the PZT30. The higher Pb content at the PZT30 surface appears correlated with the complete disappearance of the nanostructures, suggesting that the addition of Pb allows completion of the PZT reaction consuming all of the other precursors and inhibiting the formation of the chemically distinct nanostructures. The oxygen content is slightly depleted, possibly as a result of the high annealing

Table 2: PZT surface and sub-surface composition based on the XPS intensities at 90° and 30° take-off angles for both PZT10 and PZT30

	PZT10		PZT30	
	90°	30°	90°	30°
Pb	20.9	20.3	21.9	25.3
Ti	4.3	3.6	3.4	2.8
Zr(I)	11.3	7.3	2*15.6	2*14.8
Zr(II)	6.8	8.3		
O(I)	36.7	34.5	3*59.1	3*57.1
O(II)	12.4	15.7		
O(III, IV)	7.6	10.3		

temperature for crystallization. As seen in Fig. 4, both Zr_I and O_I decrease at the surface for PZT10 and at the same time the Zr_{II} and O_{II} concentrations increase. $O_{III,IV}$ are included to show that their weight also increases at the surface, consistent with the assignment to surface contamination.

The presence of the nanostructures at the grain boundaries may be understood by the fact that the formation of the perovskite phase starts from a seed and proceeds by outward, lateral growth. It then enlarges by transforming the remaining precursors into the perovskite phase between 500°C and 700°C via three dimensional growth [32]. When the lead precursor is exhausted the reaction stops abruptly. Any residual precursors remaining at the grain boundaries become available to form a secondary phase and since the TiO_2 precursor is consumed first, it is probable that the resulting secondary phase nanostructures will be at least Zr-enriched.

XRD shows that high lead excess modifies the preferential (100) orientation to a mixed state dominated by (111), in agreement with previous results [33, 34]. However, the Pb chemistry is the same at the surface of PZT30 and PZT10. Thus, despite the difference of lead excess, in both cases reacted PbO has formed the perovskite making it unlikely that the secondary phase includes Pb. Furthermore, the nanostructures appear only at the surface, they presumably form at the end of the PZT growth and therefore do not influence the crystallographic orientation.

The surface Zr content of PZT10 is 15.6% compared with 14.8% for PZT30 showing that there is slightly more Zr at the surface of PZT10. As can be seen from table II, the Zr surface enrichment is due to the Zr_{II} component. On the basis of the Zr_{II} and O_{II} core level intensities we can estimate

the ZrO_x composition. The O_{II}/Zr_{II} ratio for TOA of 90° gives x = 1.82 (i.e. $ZrO_{1.82}$), whereas at 30° the O_{II}/Zr_{II} ratio gives x = 1.89 (i.e. $ZrO_{1.89}$).

The formal valence state of Zr in both PZT and ZrO_2 is 4+. At first sight it is therefore surprising that a Zr rich surface oxide shows a distinct core level binding energy with respect to that of Zr in PZT. However, the XPS data in the literature shows that the Zr binding energy is (181.4 ±0.1) eV in PZT [10, 24, 35, 32, 36, 37, 38, 39, 40, 41, 42, 43, 44, 45, 46] and (182.4 ±0.3) eV in ZrO_2 [47, 48, 49, 50, 51, 52, 53, 54, 55, 56], in excellent agreement with the 1 eV shift measured here. Beyond the immediate chemical environment of the Zr emitter, two other effects may influence the BE shift. First, in a simple picture of electron transfer following relative electronegativity, the second neighbor interactions, could modify the electron transfer between Zr-O-Ti. Secondly, we are considering 30 nm nanostructures, with a much higher surface to volume ratio and probable shorter interatomic distances, both of which might influence the core level shift. Here some first principles calculations or even tight binding cluster calculations would be useful to confirm this interpretation.

The core level XPS analyses as a function of precursor composition, emission angle and ion beam etching therefore conclusively demonstrate that the nanostructures at the PZT10 surface are a zirconium oxide, $ZrO_{1.82-1.89}$.

The XPS results are confirmed by GID (Fig. 7b). The intensities centered on 34°, 58° and 61.5° on the PZT10 sample are not visible on the PZT30 sample and can be attributed to ZrO_2-like monoclinic structure [57]. Although weak, they are further evidence that the surface nanostructures observed on SEM may consist of a distinct phase with respect to the PZT. Using a Scherrer fit to the 61.5° peak width the diameter of grains is in the range 15 nm, in good agreement with the nanograin size estimated from the SEM image of Fig. 1(a).

ZrO_2 is a good insulator with a static dielectric constant of 25 [58] and a band gap of 5.8eV [59]. The presence of $ZrO_{1.82-1.89}$ at the PZT/electrode interface of a capacitor might well influence electrical performance. Given the higher band gap with respect to PZT, a discontinuous or continuous interfacial $ZrO_{1.82-1.89}$ layer with lower dielectric constant [60] compared to PZT (dielectric constant < 1000) [61] or a ferroelectric dead layer will decrease device capacitance. ZrO_2 is not ferroelectric, therefore a surface phase close to ZrO_2 would act like a ferroelectric dead-layer. It is not yet clear how and to what extent such a surface phase might influence the electrical characteristics. The formation of nanostructures is favored or inhibited by the Pb

excess, however, the composition of these nanostructures may have a more complex dependance on the process conditions. Systematic experiments as a function of Pb excess and for example the Ti/Zr composition profile are envisaged.

5. Conclusions

We have presented a comprehensive surface-sensitive analysis on the effects of lead amount in excess on the surface of PZT thin film. For low amount of excess lead precursor (10%), nanostructures are observed on PZT surface by SEM. Higher Pb excess (30%) inhibits nanostructure formation. Quantitative, angle-resolved XPS shows that the nanostructures are zirconium oxide, $ZrO_{1.82-1.89}$, contrary to previous studies which suggested a pyrochlore surface phase. XRD suggests a monoclinic crystal structure. Systematic studies of the effect of a nanostructured surface phase on electric characteristics as well as the interface with an electrode are currently in progress.

6. Acknowledgments

I.G. is funded by a CEA CTBU research grant. This work was performed at the Nanocharacterization Platform of CEA-MINATEC.

[1] S. Trolier-Mckinstry, P. Muralt, Thin film piezoelectrics for MEMS, Journal of Electroceramics 12 (2004) 7–17. doi:10.1023/B:JECR.0000033998.72845.51.

[2] R. E. Jones, P. Zurcher, P. Chu, D. J. Taylor, Y. T. Lii, B. Jiang, P. D. Maniar, S. J. Gillespie, Memory applications based on ferroelectric and high-permittivity dielectric thin films, Microelectronic Engineering 29 (1995) 3–10. doi:10.1016/0167-9317(95)00106-9.

[3] S. Tadigadapa, K. Mateti, Piezoelectric MEMS sensors: state-of-the-art and perspectives, Measurement Science and Technology 20 (2009) 092001. doi:10.1088/0957-0233/20/9/092001.

[4] K. A. Schönau, L. A. Schmitt, M. Knapp, H. Fuess, R.-A. Eichel, H. Kungl, M. J. Hoffmann, Nanodomain structure of Pb[Zr_{1x}Ti_{x}]O_{3} at its morphotropic phase boundary: Investigations from local to average structure (2007). doi:10.1103/PhysRevB.75.184117.

[5] R. L. Holman, R. M. Fulrath, Intrinsic nonstoichiometry in the lead zirconate-lead titanate system determined by Knudsen effusion, Journal of Applied Physics 44 (1973) (1973) 5227–5236. doi:10.1063/1.1662136.

[6] A. Etin, G. E. Shter, R. Brener, S. Baltianski, G. S. Grader, Surface composition and imprint in CSD-based PZT films, Journal of the American Ceramic Society 90 (2007) 3800–3803. doi:10.1111/j.1551-2916.2007.02056.x.

[7] B. Vaidhyanathan, A. P. Singh, D. K. Agrawal, T. R. Shrout, R. Roy, S. Ganguly, Microwave Effects in Lead Zirconium Titanate Synthesis: Enhanced Kinetics and Changed Mechanisms, Journal of the American Ceramic Society 84 (6) (2004) 1197–1202. doi:10.1111/j.1151-2916.2001.tb00816.x.
URL http://doi.wiley.com/10.1111/j.1151-2916.2001.tb00816.x

[8] T. Tani, D. a. Payne, Lead oxide coatings on sol-gel-derived lead lanthanum zirconium titanate thin layers for enhanced crystallization into the perovskite structure, Journal of the American Ceramic Society 77 (5) (1994) 1242–1248. doi:10.1111/j.1151-2916.1994.tb05398.x.

[9] Y. Park, K. W. Jeong, J. T. Song, Effect of excess Pb on fatigue properties of PZT thin films prepared by rf-magnetron sputtering, Materials Letters 56 (October) (2002) 481–485. doi:10.1016/S0167-577X(02)00536-0.

[10] A. Sachdeva, M. Kumar, V. Luthra, R. P. Tandon, Phase evolution studies of sol-gel derived lead zirconate titanate (PZT) nanopowder using X-ray diffraction and X-ray photoelectron spectroscopy, Applied Physics A: Materials Science and Processing 104 (2011) 103–108. doi:10.1007/s00339-011-6301-8.

[11] J. Wang, J. M. Xue, D. M. Wan, B. K. Gan, Mechanically Activating Nucleation and Growth of Complex Perovskites, Journal of Solid State Chemistry 328 (2000) 321–328. doi:10.1006/jssc.2000.8782.

[12] D. Liu, C. Wang, H. Zhang, J. Li, L. Zhao, C. Bai, Domain configuration and interface structure analysis of sol-gel-derived PZT ferroelectric thin films, Surface and Interface Analysis 32 (1) (2001) 27–31. doi:10.1002/sia.999.

[13] C. K. Kwok, S. B. Desu, Pyrochlore to perovskite phase transformation in sol-gel derived lead-zirconate-titanate thin films, Applied Physics Letters 60 (1992) (1992) 1430–1432. doi:10.1063/1.107312.

[14] L. A. Bursill, K. G. Brooks, Crystallization of sol-gel derived lead-zirconate-titanate thin films in argon and oxygen atmospheres, Journal of Applied Physics 75 (1994) (1994) 4501–4509. doi:10.1063/1.355941.

[15] M. Subramanian, G. Aravamudan, G. Subba Rao, Oxide pyrochlores A review, Progress in Solid State Chemistry 15 (2) (1983) 55–143. doi:10.1016/0079-6786(83)90001-8.

[16] A. D. Polli, F. F. Lange, C. G. Levi, Metastability of the fluorite, pyrochlore, and perovskite structures in the PbO-ZrO2-TiO2 system, Journal of the American Ceramic Society 83 (2000) 873–881. doi:10.1111/j.1151-2916.2000.tb01288.x.
URL <Go to ISI>://000086506800030

[17] A. Bose, M. Sreemany, Influence of processing conditions on the structure, composition and ferroelectric properties of sputtered PZT thin films on Ti-substrates, Applied Surface Science 289 (2014) 551–559. doi:10.1016/j.apsusc.2013.11.041.
URL http://dx.doi.org/10.1016/j.apsusc.2013.11.041

[18] M. S. Silva, M. Cilense, E. Orhan, M. S. Góes, M. A. C. Machado, L. P. S. Santos, C. O. Paiva-Santos, E. Longo, J. A. Varela, M. A. Zaghete, P. S. Pizani, The nature of the photoluminescence in amorphized PZT, Journal of Luminescence 111 (2005) 205–213. doi:10.1016/j.jlumin.2004.08.045.

[19] A. Etin, G. E. Shter, G. S. Grader, G. M. Reisner, Interrelation of ferroelectricity, morphology, and thickness in sol-gel-derived PbZrxTi1-xO3 films, Journal of the American Ceramic Society 90 (2007) 77–83. doi:10.1111/j.1551-2916.2006.01371.x.

[20] R. H. Liang, D. Rémiens, C. Soyer, N. Sama, X. L. Dong, G. S. Wang, Etching characteristics and absence of electrical properties damage of PZT thin films etched before crystallization, Microelectronic Engineering 85 (2008) 670–674. doi:10.1016/j.mee.2007.12.031.

[21] J. L. Wang, F. Gaillard, A. Pancotti, B. Gautier, G. Niu, B. Vilquin, V. Pillard, G. L. M. P. Rodrigues, N. Barrett, Chemistry and atomic distortion at the surface of an epitaxial BaTiO 3 thin film after dissociative adsorption of water, Journal of Physical Chemistry C 116 (001) (2012) 21802–21809. doi:10.1021/jp305826e.

[22] G. N. Greaves, N. T. Barrett, G. M. Antonini, F. R. Thornley, B. T. Willis, A. Steel, Glancing angle X-Ray absorption spectroscopy of corroded Borsilicate glass surfaces containg Uranium, J. Am. Chem. Soc. 111 (22) (1989) 4313–4324. doi:10.1021/ja00194a024.
URL http://pubs.acs.org/doi/abs/10.1021/ja00194a024

[23] L. G. Parratt, Surface studies of solids by total reflection of x-rays, Physical Review 95 (2) (1954) 359–369. doi:10.1103/PhysRev.95.359.

[24] J. K. Lee, T.-y. Kim, I. Chung, S. B. Desu, Characterization and elimination of dry etching damaged layer in Pt/Pb(Zr[sub 0.53]Ti[sub 0.47])O[sub 3]/Pt ferroelectric capacitor, Applied Physics Letters 75 (1999) (1999) 334–336. doi:10.1063/1.124367.
URL http://link.aip.org/link/APPLAB/v75/i3/p334/s1&Agg=doi

[25] J. D. Baniecki, M. Ishii, T. Shioga, K. Kurihara, S. Miyahara, Surface core-level shifts of strontium observed in photoemission of barium strontium titanate thin films, Applied Physics Letters 89 (16) (2006) 162908. doi:10.1063/1.2357880.
URL http://link.aip.org/link/APPLAB/v89/i16/p162908/s1&Agg=doi

[26] J. N. Kim, K. S. Shin, D. H. Kim, B. O. Park, N. K. Kim, S. H. Cho, Changes in chemical behavior of thin film lead zirconate titanate during Ar+-ion bombardment using XPS, Applied Surface Science 206 (2003) 119–128. doi:10.1016/S0169-4332(02)01229-1.

[27] S. A. Chambers, T. Droubay, T. C. Kaspar, M. Gutowski, M. van Schilfgaarde, Accurate valence band maximum determination for SrTiO3(001), Surface Science 554 (2-3) (2004) 81–89.

[28] T. J. Zhu, X-ray diffraction and photoelectron spectroscopic studies of (001)-oriented Pb(Zr[sub 0.52]Ti[sub 0.48])O[sub 3] thin films prepared by laser ablation, Journal of Applied Physics 95 (001) (2004) 241.

doi:10.1063/1.1631750.
URL http://scitation.aip.org/content/aip/journal/jap/95/1/10.1063/1.1631750\n

[29] A. Zomorrodian, A. Mesarwi, N. J. Wu, A. Ignatiev, XPS oxygen line broadening in lead zirconium titanate and related materials, Applied Surface Science 90 (1995) 343–348. doi:10.1016/0169-4332(95)00155-7.

[30] J. Abergel, M. Allain, H. Michaud, M. Cueff, T. Ricart, C. Dieppedale, G. Le Rhun, D. Faralli, S. Fanget, E. Defay, Optimized gradient-free PZT thin films for micro-actuators, in: IEEE International Ultrasonics Symposium, IUS, 2012, pp. 972–974. doi:10.1109/ULTSYM.2012.0243.

[31] S. A. Impey, Z. Huang, A. Patel, R. Beanland, N. M. Shorrocks, R. Watton, R. W. Whatmore, Microstructural characterization of sol-gel lead–zirconate–titanate thin films, Journal of Applied Physics 83 (1998) (1998) 2202. doi:10.1063/1.366957.
URL http://scitation.aip.org/content/aip/journal/jap/83/4/10.1063/1.366957

[32] N. Wakiya, K. Kuroyanagi, Y. Xuan, K. Shinozaki, N. Mizutani, XPS study of the nucleation and growth behavior of an epitaxial Pb(Zr,Ti)O3/MgO(100) thin film prepared by MOCVD, Thin Solid Films 372 (2000) 156–162. doi:10.1016/S0040-6090(00)01013-0.
URL http://www.sciencedirect.com/science/article/pii/S0040609000010130

[33] C. Soyer, E. Cattan, D. Rèmiens, Ion beam etching of PZT thin films: Influence of grain size on the damages induced, Journal of the European Ceramic Society 25 (2005) 2269–2272. doi:10.1016/j.jeurceramsoc.2005.03.043.

[34] C. S. Park, J. W. Lee, S. M. Lee, S. H. Jun, H. E. Kim, Effect of excess PbO on microstructure and orientation of PZT(60/40) films, Journal of Electroceramics 25 (2010) 20–25. doi:10.1007/s10832-009-9584-9.

[35] R. Vaidya, R. J. Simonson, J. Cesarano, D. Dimos, G. P. López, Formation and Stability of Self-Assembled Monolayers on Thin Films of Lead Zirconate Titanate (PZT), Langmuir 12 (22) (1996) 2830–2836. doi:10.1021/la951072k.
URL http://pubs.acs.org/doi/abs/10.1021/la951072k

[36] N. G. Apostol, L. E. Stoflea, G. A. Lungu, L. C. Tanase, C. Chirila, L. Frunza, L. Pintilie, C. M. Teodorescu, Band bending in

Au/Pb(Zr,Ti)O3 investigated by X-ray photoelectron spectroscopy: Dependence on the initial state of the film, Thin Solid Films 545 (2013) 13–21. doi:10.1016/j.tsf.2013.04.092.

[37] N. G. Apostol, L. E. Stoflea, G. A. Lungu, C. Chirila, L. Trupina, R. F. Negrea, C. Ghica, L. Pintilie, C. M. Teodorescu, Charge transfer and band bending at Au/Pb(Zr0.2Ti0.8)O3 interfaces investigated by photoelectron spectroscopy, Applied Surface Science 273 (2013) 415–425. doi:10.1016/j.apsusc.2013.02.056.
URL http://dx.doi.org/10.1016/j.apsusc.2013.02.056 http://linkinghub.elsevier.com/retrieve/pii/S0169433213003747

[38] M. M. Zhu, Z. H. Du, J. Ma, Defect enhanced optic and electro-optic properties of lead zirconate titanate thin films, AIP Advances 1 (4) (2011) 042144. doi:10.1063/1.3664137.

[39] M. H. Tang, J. Zhang, X. L. Xu, H. Funakubo, Y. Sugiyama, H. Ishiwara, J. Li, Electrical properties and x-ray photoelectron spectroscopy studies of Bi(Zn[sub 0.5]Ti[sub 0.5])O[sub 3] doped Pb(Zr[sub 0.4]Ti[sub 0.6])O[sub 3] thin films, Journal of Applied Physics 108 (2010) (2010) 84101. doi:10.1063/1.3499305.
URL http://link.aip.org/link/JAPIAU/v108/i8/p084101/s1&Agg=doi

[40] S. W. Lee, S. H. Joo, S. L. Cho, Y. H. Son, K. M. Lee, S. D. Nam, K. S. Park, Y. T. Lee, J. S. Seo, Y. D. Kim, A. N. Hyeong-Geun, H. J. Kim, Y. J. Jung, J. E. Heo, M. S. Lee, S. O. Park, U. I. Chung, J. T. Moon, Plasma-assisted dry etching of ferroelectric capacitor modules and application to a 32M ferroelectric random access memory devices with submicron feature sizes, Japanese Journal of Applied Physics 41 (11 B) (2002) 6749–6753. doi:10.1143/JJAP.41.6749.

[41] S. Takatani, H. Miki, K. Kushida-Abdelghafar, K. Torii, Pt/PbZrxTi1-xO3 interfacial reaction and Schottky barrier formation studied by x-ray photoelectron spectroscopy: Effect of H-2 and O-2 annealing, Journal of Applied Physics 85 (1999) (1999) 7784–7791. doi:10.1063/1.370585.
URL <Go to ISI>://WOS:000080354300040

[42] M. G. Kang, K. T. Kim, C. I. Kim, Recovery of plasma-induced damage in PZT thin film with O2 gas annealing, Thin Solid Films 398-399 (2001) 448–453. doi:10.1016/S0040-6090(01)01463-8.

[43] A. C. Galca, V. Stancu, M. A. Husanu, C. Dragoi, N. G. Gheorghe, L. Trupina, M. Enculescu, E. Vasile, Substrate-target distance dependence of structural and optical properties in case of Pb(Zr,Ti)O3 films obtained by pulsed laser deposition, Applied Surface Science 257 (14) (2011) 5938–5943. doi:10.1016/j.apsusc.2011.01.056.
URL http://dx.doi.org/10.1016/j.apsusc.2011.01.056

[44] D. W. Zeng, K. Li, K. C. Yung, H. L. W. Chan, C. L. Choy, C. S. Xie, UV laser micromachining of piezoelectric ceramic using a pulsed Nd:YAG laser, Applied Physics A: Materials Science & Processing 78 (2004) 415–421. doi:10.1007/s00339-002-1956-9.

[45] Y. Y. Lin, Q. Liu, T. A. Tang, X. Yao, XPS analysis of Pb(Zr0.52Ti0.48)O3 thin film after dry-etching by CHF3 plasma, Applied Surface Science 165 (2000) 34–37. doi:10.1016/S0169-4332(00)00316-0.

[46] C. Dragoi, N. G. Gheorghe, G. A. Lungu, L. Trupina, A. G. Ibanescu, C. M. Teodorescu, X-ray photoelectron spectroscopy of pulsed laser deposited Pb(Zr,Ti)O3δ, Physica Status Solidi (a) 209 (6) (2012) 1049–1052. doi:10.1002/pssa.201127740.
URL http://doi.wiley.com/10.1002/pssa.201127740

[47] Y. Gao, L. Zhang, Y. Pan, G. Wang, Y. Xu, W. Zhang, J. Zhu, Epitaxial growth of ultrathin ZrO2(111) films on Pt(111), Chinese Science Bulletin 56 (6) (2011) 502–507. doi:10.1007/s11434-010-4309-7.

[48] H.-S. Kim, J.-C. Woo, Y.-H. Joo, C.-I. Kim, The Use of Inductively Coupled CF 4 /Ar Plasma to Improve the Etch Rate of ZrO 2 Thin Films, Transactions on Electrical and Electronic Materials 14 (1) (2013) 12–15. doi:10.4313/TEEM.2013.14.1.12.
URL http://koreascience.or.kr/journal/view.jsp?kj=E1TEAO&py=2013&vnc=v14n1&sp

[49] R. M. D. Física, D. Federal, Structural changes in ZrO x N y / ZrO 2 coatings deposited through spray pyrolisis-nitriding, Revista Mexicana de Física 60 (2014) 233–242.

[50] G. I. Cubillos, M. Bethencourt, J. J. Olaya, J. E. Alfonso, J. F. Marco, The influence of deposition temperature on microstructure

and corrosion resistance of ZrOxNy/ZrO2 coatings deposited using RF sputtering, Applied Surface Science 309 (2014) 181–187. doi:10.1016/j.apsusc.2014.04.215.
URL http://dx.doi.org/10.1016/j.apsusc.2014.04.215 http://linkinghub.elsevier.com/retrieve/pii/S0169433214010071

[51] R. Brenier, J. Mugnier, E. Mirica, XPS study of amorphous zirconium oxide films prepared by sol-gel, Applied Surface Science 143 (1999) 85–91. doi:10.1016/S0169-4332(98)00901-5.

[52] Y. Pan, Y. Gao, D. Kong, G. Wang, J. Hou, S. Hu, H. Pan, J. Zhu, Interaction of Au with thin ZrO2 films: influence of ZrO2 morphology on the adsorption and thermal stability of Au nanoparticles., Langmuir 28 (2012) 6045–6051. doi:10.1021/la205104q.
URL http://www.ncbi.nlm.nih.gov/pubmed/22424149

[53] V. R. Chinchamalatpure, Synthesis and Electrical Characterization of ZrO2 Thin Films on Si(100), Journal of Modern Physics 03 (January) (2012) 69–73. doi:10.4236/jmp.2012.31010.

[54] J.-C. Woo, S.-G. Kim, J.-G. Koo, G.-H. Kim, D.-P. Kim, C.-H. Yu, J.-Y. Kang, C.-I. Kim, A study on dry etching for profile and selectivity of ZrO2 thin films over Si by using high density plasma, Thin Solid Films 517 (14) (2009) 4246–4250. doi:10.1016/j.tsf.2009.02.012.
URL http://dx.doi.org/10.1016/j.tsf.2009.02.012

[55] L. M. Eshelman, A. M. de Jong, J. W. Niemantsverdriet, Preparation of ZrO2 on flat, conducting SiO2/Si(100) model supports by wet chemical techniques; X-ray photoelectron spectroscopy and Auger depth profiling, Catalysis Letters 10 (1991) 201–209. doi:10.1007/BF00772072.

[56] J.-C. Woo, C.-A. Choi, W.-S. Yang, Y.-S. Chun, C.-I. Kim, Surface properties of ZrO2 thin film under Cl2 / Ar plasma using angle-resolved X-ray photoelectron spectroscopy Surface properties of ZrO 2 thin fi lm under Cl 2 / Ar plasma, Japanese Journal of Applied Physics 53 (2014) 08NB05.

[57] C. Lin, C. Zhang, J. Lin, Phase transformation and photoluminescence properties of nanocrystalline ZrO2 powders prepared via the pechini-type sol-gel process, Journal of Physical Chemistry C 111 (2007) 3300–3307. doi:10.1021/jp066615l.

[58] J. Robertson, High density plasma enhanced chemical vapor deposition of optical thin films, The European Physical Journal Applied Physics 28 (2004) 265–291. doi:10.1051/epjap.

[59] P. W. Peacock, J. Robertson, Band offsets and Schottky barrier heights of high dielectric constant oxides, Journal of Applied Physics 92 (2002) (2002) 4712–4721. doi:10.1063/1.1506388.

[60] C. Soyer, E. Cattan, D. Rèmiens, M. Guilloux-Viry, Ion beam etching of lead-zirconate-titanate thin films: Correlation between etching parameters and electrical properties evolution, Journal of Applied Physics 92 (2002) (2002) 1048–1055. doi:10.1063/1.1476970.

[61] R. Moazzami, C. Hu, W. H. Shepherd, Electrical characteristics of ferroelectric PZT thin films for DRAM applications, IEEE Transactions on Electron Devices 39 (9) (1992) 2044–2049. doi:10.1109/16.155876.